Designing, fabricating, and imaging Raman hot spots

Lidong Qin*, Shengli Zou*, Can Xue, Ariel Atkinson, George C. Schatz†, and Chad A. Mirkin‡

Department of Chemistry and International Institute for Nanotechnology, Northwestern University, 2145 Sheridan Road, Evanston, IL 60208-3113

Contributed by George C. Schatz, July 13, 2006

We have developed a probe of the electromagnetic mechanism of surface-enhanced Raman scattering via Au nanodisk arrays generated by using on-wire lithography. In this approach, disk thickness and interparticle gap are precisely controlled from 5 nm to many micrometers. Confocal Raman microscopy demonstrates that disk thickness and gap play a crucial role in determining surface-enhanced Raman scattering intensities. Theoretical calculations also demonstrate that these results are consistent with the electromagnetic mechanism, including the surprising result that the largest enhancement does not occur for the smallest gaps.

electromagnetic mechanism | nanofabrication | surface-enhanced Raman scattering | templated synthesis | discrete dipole approximation

On-wire lithography (OWL) allows one to fabricate unique one-dimensional structures that cannot be prepared via any other lithographic method (1–3). In particular, it allows one to make nanodisk arrays coated on one side with a thin silica sheath where the disk composition, thickness, and separation along the long axis can be controlled with nanometer precision. This ability enables the exploration of a variety of chemical and physical phenomena, including plasmon coupling and electromagnetic field enhancement in a very unique manner. Electromagnetic field enhancement is, in part, the basis behind surface-enhanced Raman scattering (SERS), a spectroscopic phenomenon discovered over 30 years ago but still perplexing to the scientific community both in terms of its potential and scientific origins (4–27). Two mechanisms are often mentioned in the literature, (6) the electromagnetic mechanism and the chemical mechanism. The latter involves charge transfer excitation (7, 9) between analyte molecules and the metal particles, whereas the former is dominated by plasmon excitation leading to hot spots around nano-sized metal particles (10, 13–25). A challenge in characterizing the electromagnetic mechanism is the difficulty associated with making nanoparticle structures with controllable interparticle gaps and doing so in a way that does not significantly change chemical composition. Because of this problem, it would be particularly useful to be able to make a series of nearly identical nanostructures with controllable gap size that can be probed simultaneously under one set of conditions in a SERS experiment. By designing the experiment in this manner, differences in chemical enhancement are minimized, and one can focus on the relationship between nanostructure and electromagnetic enhancement. Here, we show how OWL can be used to systematically prepare rows of Au disks with precisely controlled thicknesses and gaps, enabling a combinatorial format for identifying structures that provide maximum SERS enhancement.

Nanodisk arrays fabricated by OWL are particularly useful for preparing SERS-active nanostructures for the following reasons. (*i*) Multiple features can be synthesized within a single nanowire, and, once functionalized with a SERS-active molecule, these features can be individually addressed and probed for SERS response and probed within the context of a single experiment. (*ii*) The gap distances between nanodisks can be tuned between 5 nm and 8 μm; thus, the coupling between nanodisks can be systematically studied over regimes that range from near-field to diffractive interactions. Neither conventional lithography nor colloid particle assembly techniques are capable of routinely producing comparable structures over this size range. (*iii*) The disk thickness (Au in this case) can be controlled from 20 nm to many micrometers. This range allows one to produce structures with localized surface plasmon resonance wavelengths that span 550 nm to >1,000 nm. Below 20 nm, the cohesive interaction between the SiO_2 coating and the disks is not large enough to keep them from collapsing.

Results and Discussion

To evaluate the prospect of using OWL-fabricated nanowires for SERS hot spot studies, we designed a series of structures with an identical gap size and variable disk thicknesses as well as an identical disk thickness and variable gap sizes. We studied gap sizes ranging from 5 to 360 nm with a fixed disk thickness of 120 or 300 nm and thicknesses ranging from 40 to 600 nm with a fixed gap distance of 30 nm. Note that all of the Au nanodisks used in this study had a fixed diameter of 360 nm. Forty-six different nanodisk array structures were studied with a confocal Raman microscope. Through these initial studies, we identified some common features, including gap numbers, disk thicknesses, and gap sizes that determine high SERS activity.

Field emission SEM images of the initial structures clearly showed the alternating Au (bright contrast) and Ni (dark contrast) segments in each wire (Fig. 1 *A–C*). After the OWL process, the Ni segments were completely removed (Fig. 1 *D–F*). Energy dispersed x-ray analysis of the structures also were consistent with this conclusion. The yield of the described structures is in the milligram range with over a billion structures produced from one template (Fig. 4, which is published as supporting information on the PNAS web site). The disk array products can be suspended easily in solvents such as ethanol, methanol, or water. Methylene blue (MB) was selected as the Raman probe molecule for these studies because it adsorbs onto Au and exhibits little fluorescence background signal (Fig. 5, which is published as supporting information on the PNAS web site).

The confocal Raman microscopy results provided several pieces of useful information. First, individual disks show little enhancement compared with disk structures with gaps (Fig. 2). Note that the individual disk is located far left in Fig. 2 *A* and *D*. For a fixed gap size of 30 nm, the number of gaps does not significantly affect the measured enhancement (Fig. 2 *A* and *D*). The spot sizes become slightly larger when gap number increases because of the larger disk array surface area, but the intensities vary by less than a factor of 2. Note, however, that the signal for two disks with one gap is 167 times higher than that from one disk without a gap (Fig. 1*D*, left side of image). Second, when the disk thickness is varied and the gap size is kept constant at 30 nm, significant variations in SERS activity are observed. As a representative example, we show the results from four different disk thicknesses of 40 ± 5, 80 ± 8, 120 ± 10, and 200 ± 15 nm with

Conflict of interest statement: No conflicts declared.

Abbreviations: OWL, on-wire lithography; SERS, surface-enhanced Raman scattering; MB, methylene blue.

*L.Q. and S.Z. contributed equally to this work.

†To whom correspondence on theoretical work should be addressed. E-mail: schatz@chem.northwestern.edu.

‡To whom correspondence on experimental work should be addressed. E-mail: chadnano@northwestern.edu.

www.pnas.org/cgi/doi/10.1073/pnas.0605889103

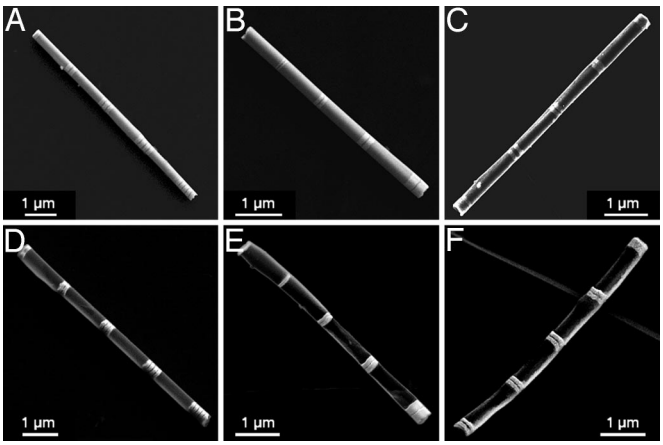

Fig. 1. Field emission SEM images of nanowires and corresponding nanodisk arrays. (*A*) Identical 120- ± 10-nm Au disks with 30- ± 5-nm Ni separations. (*B*) Au disk with identical 30- ± 5-nm Ni separations and thicknesses of 40 ± 5, 80 ± 8, 120 ± 10, and 200 ± 15 nm from top left to bottom right. At the top left is a single Au disk (thickness = 40 nm). (*C*) Identical 120- ± 10-nm Au disks with Ni segments of 160 ± 10, 80 ± 10, 30 ± 5, 15 ± 5, and 5 ± 2 nm from bottom left to top right. (*D–F*) SEM images of the gapped nanowire structures after performing the OWL process on *A* (*D*) *B* (*E*), and *C* (*F*). Separations between groups of Au nanodisks are ≈1 μm in all nanowires.

a single 30 nm gap (Fig. 1 *B* and *E*). A single 40 ± 5 nm disk with no gap is placed at the end of the structure as a control (Fig. 1*E*, left side of image). Interestingly, a 120-nm-thick disk yields the largest SERS response, followed by disks measuring 200, 80, and 40 nm. Finally, we studied a disk array with the disk thickness optimized at 120 nm and gap size deliberately varied from 5 ± 2 to 15 ± 5, 30 ± 5, 80 ± 10, and 160 ± 10 nm (Fig. 1 *C* and *F*; see also Fig. 6, which is published as supporting information on the PNAS web site). The SERS data show that the optimum gap size is 30 nm (Fig. 2 *C* and *F*), consistent with the previous experiments, in which gap size was kept constant and disk thickness was varied (Fig. 2*E*). These observations lead one to conclude for these Au disk arrays that maximum SERS enhancement occurs for 120-nm-thick disks with 30-nm gaps.

The observations and conclusion above are notable for a couple of reasons. First, although it is difficult to generate nanostructures with stable and comparable SERS activities, the OWL structures exhibit extremely consistent SERS results from batch to batch, and the magnitude of enhancement is consistent with other molecules (*p*-mercaptobenzoic acid) studied in separate but analogous experiments. Second, many studies lead one to believe that exceedingly small structures and gaps (<10 nm) are required to generate the hot spots typically associated with high SERS activity (24, 27). Therefore, it is surprising that 120-nm disks are better than smaller structures and 30-nm gaps lead to higher activities than 5- or 15-nm gaps.

To interpret the observed results in terms of the electromagnetic mechanism of SERS, we have calculated the local electric fields $|E|^2$ between disk dimers in vacuum using the discrete dipole approximation method. (26, 28) The resulting contours at 633 nm are shown in Fig. 3. Each column represents dimers with identical disk thicknesses and varied gap separations of 5, 10, 15, 30, and 80 nm, and each row represents dimers with identical gap distances and varied thicknesses of 40, 80, 120, 160, and 200 nm. The 120-nm-thick disks show the largest peak electric fields ($|E|^4$ maximizes at 10^5 times the incident field intensity) and the highest average fields ($\langle|E|^4\rangle = 2{,}517$, where the average is over the entire surface area of both particles). This dependence of the results on disk thickness is in excellent agreement with the experimental measurements (Fig. 2*E*). We also find that the magnitude of the SERS enhancement factor compared with that for an isolated disk (where $\langle|E|^4\rangle = 38$) is fairly accurately predicted [the calculated ratio is $2{,}517/38 \approx 66$, whereas the measured ratio is $\approx 500/(\approx 3\text{–}5) \approx 125$]. Previously, Hao and Schatz (19) studied the electric fields around silver nano triangles and found that the electric fields between them increased dramatically with decreasing gap distance. However, in the present simulation, the electric fields (both peak and average) are found to peak for a 10-nm gap. For example, $\langle|E|^4\rangle$ is 2,517 for 120-nm-thick disks with a 10-nm gap, 642 when the gap distance is 5 nm, and 339 when the gap is 15 nm. These results are in qualitative agreement with the experimental observations, except that the highest Raman signals occur when the gap is 30 nm. Although gaps between particles generally lead to enhanced fields, the decline in enhancement for very small gaps arises because the dipole plasmon mode is detuned to the red of the

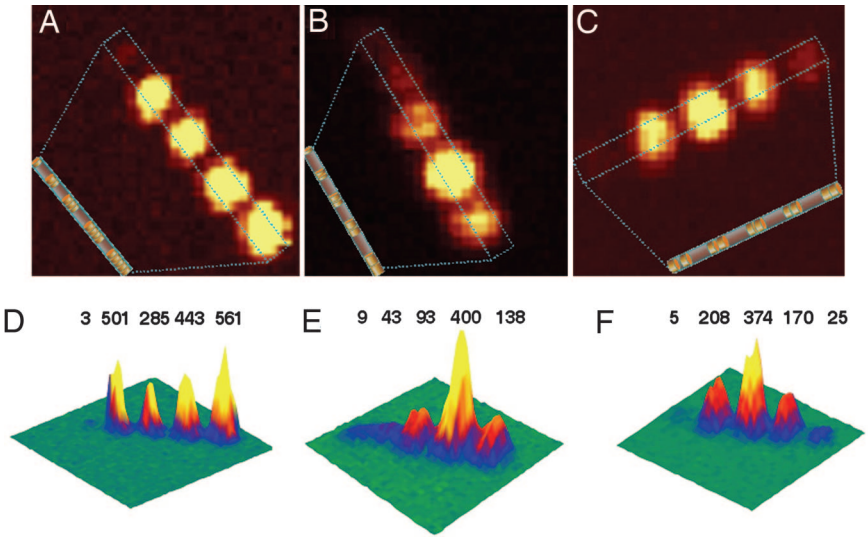

Fig. 2. Confocal Raman microscopy images of gapped nanowire structures functionalized with MB. (*A–C*) Two-dimensional Raman images corresponding to the structures shown in Fig. 1 *D* (*A*), E (*B*), and *F* (*C*). (*D–F*) Three-dimensional Raman images. *A Inset*, *B Inset*, and *C Inset* are schematic representations of the structures being imaged. Peak intensities are in arbitrary units.

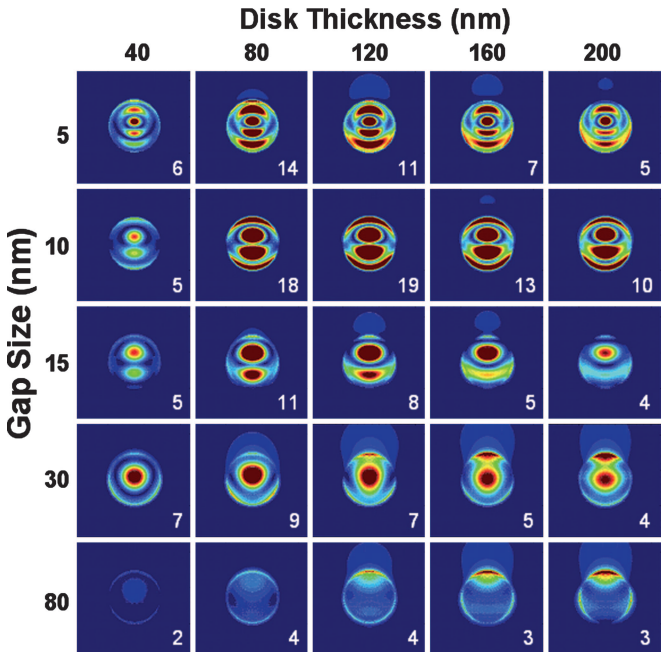

Fig. 3. Electric field enhancement (contours of $|E|^2$) for disk dimers composed of identical Au disks with different thicknesses and gap distances. In columns 1–5, the disk thicknesses are 40, 80, 120, 160, and 200 nm, respectively. In rows 1–5, the gap distances are 5, 10, 15, 30, and 80 nm, respectively. Contours vary from 0 (blue) to 50 (red) times the incident field intensity. The number in the lower right corner of each image is $|E|^2$ relative to the isolated particle result.

excitation and Stokes-shifted wavelengths. This phenomenon is apparent from Fig. 3, which shows an increased number of nodes in the field as the gap is decreased due to excitation of higher multipoles. Although the higher multipoles still produce strong scattering at 633 nm, the field enhancements associated with these modes are smaller than for the dipole mode because of their depolarized (partially out of phase) response. We also find that the optimum disk size of 120 nm is a compromise between disks that are too thick to allow light to penetrate into the gap (for disks >120 nm) and disks that are too thin to effectively confine the field into the gap region (for disks <120 nm). Of course, the situation is more complicated in the experiment because of the surface roughness in the gap. There is also some error in the calculations due to the large grid spacing needed to enable studies of these large structures. However, it is encouraging that theory and experiment are in semiquantitative agreement.

The present results provide important insights concerning the role of the electromagnetic mechanism in SERS. In contrast to earlier experimental and theoretical work that suggested that the SERS enhancement is largest for junctions with the smallest gap (10, 13–25), here we find a non-zero optimum gap size for a specified excitation wavelength that results from the red-shifting of the dipole plasmon wavelength as gap size is decreased. Second, we show that there is also an optimum particle size that reflects the ability of light to penetrate into and be confined by the gap structure. Third, the observed SERS enhancement factor of $\approx$100 times that for isolated disks agrees well with theory, providing one of the few quantitative confirmations of the electromagnetic mechanism for a well defined metal nanostructure. Finally, we demonstrate the OWL process for producing and optimizing well defined dispersible substrates with tailorable and highly reproducible plasmonic coupling properties. These types of structures will be of utility in a variety of spectroscopic encoding and biological and chemical sensing applications (29–32).

Materials and Methods

Materials. Multisegment nanowires and nanodisk arrays were prepared according to literature methods (1). In all experiments, commercially available nickel sulfamate SEMI Bright RTU (Ni) and Orotemp 24RTU (Au) from Technic, Inc. (Irving, TX) were used for electrochemical deposition. For growth of Ni segments thicker than 10 nm, a −900-mV deposition potential (Ag/AgCl reference, Pt counter electrode) was used. To precisely deposit segment lengths of 5 nm, we diluted the Ni plating solution by a factor of 100 and applied a −780-mV potential. Note that careful rinsing of the electrochemical deposition cell was required when changing Au and Ni plating solutions.

We controlled the number of coulombs passed during electrochemical deposition to achieve a desired nanowire structure. The charge and length of each sample are shown in Table 1, which is published as supporting information on the PNAS web site. We characterized the nanowire structures before and after the OWL process, which first coats the Au–Ni multisegment nanowire formed from hard template synthesis with a 50-nm layer of silica. Then, the sacrificial Ni segments were dissolved, resulting in gaps along the long axis of the nanowire. The resulting structures were characterized by SEM (Fig. 1). Large-area optical images of the nanodisk arrays are shown in Fig. 4. Fig. 4 *A*, *B*, and *C* correspond to Fig. 1 *D*, *E*, and *F*, respectively. The bright spots represent the segments composed of Au nanodisks and the small gaps. The dark areas are the large gaps between the nanodisk/gap arrays. These Au disks are bridged with the half coating of SiO_2, which keeps them at a well defined distance. Some gapped nanowires aggregate during drying before the optical measurements and appear very bright in these images.

The growth of Au and Ni segments follows Faraday's law of electrolysis (1). For example, in Fig. 1*C*, we controlled the deposition of Ni segments to adjust the distance between the Au nanodisks. Charges of 1.332, 0.666, 0.251, 0.080, and 0.040 C were applied during electrochemical deposition (Table 1). The resulting Ni segment lengths were 160, 80, 30, 15, and 5 nm, respectively. Fig. 1*C* also shows that the dark stripes between the bright regions are get progressively thinner from the bottom left to the upper right. Zoomed-in images of the two thinnest stripes are shown in Fig. 6. The Ni segments are marked in between arrows.

Au Nanodisk Array Functionalization (e.g., MB). To effectively modify the surface with MB, the disk arrays were isolated from an ethanol solution by centrifugation and resuspended in a 1 μM ethanol solution of MB and then shaken overnight at speed 6 in a Roto-Shake Genie SI-1100 (Scientific Industries, Bohemia, NY). The MB-modified disk arrays were isolated by centrifugation and repeatedly washed with ethanol to remove free and physisorbed MB. The disk arrays were then cast onto piranha-pretreated glass substrates and characterized by scanning confocal Raman microscopy (Fig. 2). The incident laser wavelength was 633 nm, and the intense C–C ring stretch mode of MB at 1,621 cm^{-1} was recorded as a function of position along the long axis of the disk array. The microscopic length of the wire allows one to spectroscopically address and distinguish each set of nanodisk structures independently.

Confocal Raman Microscope. Raman spectra and images were recorded with a confocal Raman microscope (CRM200 WiTec) equipped with a piezo scanner and ×100 microscope objectives (n.a. = 0.90; Nikon, Tokyo, Japan). The spatial resolution is as high as 400 nm in this experiment.

Samples were excited with a 632.8-nm He–Ne laser (Coherent,

Inc., Santa Clara, CA) with a spot size of ≈1 μm and a power density of ≈10^4 W/cm^2 incident on the samples. For a typical Raman image with a scan range of 10 × 10 μm, complete Raman spectra were acquired on every pixel with an integration time of 0.1 second per spectrum and an image resolution of 100 pixels × 100 lines. To provide a careful analysis of the enhanced Raman scattering signal of MB on the sample features, all images presented here were processed by integrating the intensity of the Raman spectra at 1,621 cm^{-1}. The SERS spectra of both MB and *p*-mercaptobenzoic acid with different concentrations were obtained with 1-s integration time. MB shows a strong absorption band at ≈655 nm, which increases the SERS signal intensity under excitation at 632.8 nm.

Theoretical Modeling. To interpret the observed results in terms of the electromagnetic mechanism of SERS, we calculated the Raman enhancement factors $|E|^4$ associated with cylindrical Au disk dimers in vacuum using the discrete dipole approximation method (26, 28) (Table 2, which is published as supporting information on the PNAS web site). The plane used for the contour in Fig. 3 is taken to be between the two disks, parallel to the disk surface, and 5 nm from one surface. The contours range from 0 to 50 times the incident intensity. The SiO_2 film is not included in these calculations, so there will be a small blue shift in plasmon resonance wavelengths from the model compared with those from the experiments; however, otherwise the model structures are chosen to be realistic. The working wavelength used in calculating the enhanced local electric fields between Au disk dimers is chosen to be the excitation wavelength of 633 nm in what we present. We also have examined results at 669 nm (the mean of the incident and Stokes-shifted wavelengths) and the results are similar. The grid size used in the discrete dipole approximation program was 5 nm. We have studied polarizations both parallel and perpendicular to the interdimer axis, which we denote as the *z* and *y* axes, respectively. For a disk diameter of 360 nm, the resonance wavelengths for these two polarizations are similar. However the SERS enhancements are large only for *z* polarization, and the variation of *z*-polarized resonance behavior with interdisk spacing is crucial to the interpretation of the experiments.

This work was supported by the U.S. Air Force Office of Scientific Research and the National Science Foundation. C.A.M. is supported financially by the Office of Naval Research and is the recipient of a National Institutes of Health Director's Pioneer Award.

1. Qin, L., Park, S., Huang, L. & Mirkin, C. A. (2005) *Science* **309,** 113–115.
2. Martin, C. R. & Baker, L. A. (2005) *Science* **309,** 67–68.
3. Gates, B. D., Xu, Q., Stewart, M., Ryan, D., Willson, C. G. & Whitesides, G. M. (2005) *Chem. Rev.* **105,** 1171–1196.
4. Fleischman, M., Hendra, P. J. & McQuillan, A. J. (1974) *Chem. Phys. Lett.* **26,** 163–166.
5. Jeanmaire, D. L. & Van Duyne, R. P. (1977) *J. Electroanal. Chem.* **84,** 1–20.
6. Dornhaus, R., Long, M. B., Benner, R. E. & Chang, R. K. (1980) *Surf. Sci.* **93,** 240–262.
7. Adrian, F. J. (1982) *J. Chem. Phys.* **77,** 5302–5314.
8. Moskovits, M. (1985) *Rev. Mod. Phys.* **57,** 783–826.
9. Yamada, H., Nagata, H., Toba, K. & Nakao, Y. (1987) *Surf. Sci.* **182,** 269–286.
10. Freeman, R. G., Grabar, K. C., Allison, K. J., Bright, R. M., Davis, J. A., Guthric, A. P., Hommer, M. B., Jackson, M. A., Smith, P. C., Walter, D. G. & Natan, M. J. (1995) *Science* **267,** 1629–1632.
11. Kneipp, K., Wang, Y., Kneipp, H., Perelman, L. T., Etzkan, I., Dasari, R. R. & Feld, M. S. (1997) *Phys. Rev. Lett.* **78,** 1667–1670.
12. Nie, S. & Emory, S. R. (1997) *Science* **275,** 1102–1106.
13. Xu, H., Bjerneld, E. J., Kall, M. & Borjesson, L. (1999) *Phys. Rev. Lett.* **83,** 4357–4360.
14. Michaels, A. M., Jiang, J. & Brus, L. (2000) *J. Phys. Chem. B* **104,** 11965–11971.
15. Gunnarsson, L., Bjerneld, E. J., Xu, H., Petronia, S., Kasemo, B. & Kall, M. (2001) *Appl. Phys. Lett.* **78,** 802–804.
16. Futamata, M., Maruyama, Y. & Ishikawa, M. (2003) *J. Phys. Chem. B* **107,** 7607–7617.
17. Jiang, J., Bosnick, K., Maillard, M. & Brus, L. (2003) *J. Phys. Chem. B* **107,** 9964–9972.
18. Fromm, D. P., Sundaramurthy, A., Schuck, P. J., Kino, G. & Moerner, W. E. (2004) *Nano Lett.* **4,** 957–961.
19. Hao, E. & Schatz, G. C. (2004) *J. Chem. Phys.* **120,** 357–366.
20. Zou, S. & Schatz, G. C. (2004) *Chem. Phys. Lett.* **403,** 62–67.
21. Talley, C. E., Jackson, J. B., Oubre, C., Grady, N. K., Hollars, C. W., Lane, S. M., Huser, T. R., Nordlander, P. & Halas, N. J. (2005) *Nano Lett.* **5,** 1569–1574.
22. Orendorff, C. J., Gole, A., Sau, T. K. & Murphy, C. J. (2005) *Anal. Chem.* **77,** 3261–3266.
23. Oubre, C. & Nordlander, P. (2005) *J. Phys. Chem. B* **109,** 10042–10051.
24. Wang, H., Levin, C. S. & Halas, N. J. (2005) *J. Am. Chem. Soc.* **127,** 14992–14993.
25. Lee, S. J., Morrill, A. R. & Moskovits, M. (2006) *J. Am. Chem. Soc.* **128,** 2200–2201.
26. Kelly, K. L., Coronado, E., Zhao, L. & Schatz, G. C. (2003) *J. Phys. Chem. B* **107,** 668–677.
27. Haynes, C. L., McFarland, A. D. & Van Duyne, R. P. (2005) *Anal. Chem.* **77,** 338A–346A
28. Draine, B. T. & Flatau, P. J. (2003) ArXiv: astro-ph/0309069.
29. Cao, Y. W. C., Jin, R. C. & Mirkin, C. A. (2002) *Science* **297,** 1536–1540.
30. Kneipp, J., Kneipp, H., Rice, W. L. & Kneipp, K. (2005) *Anal. Chem.* **77,** 2381–2385.
31. Lu, Y., Liu, G. L., Kim, J., Mejia, Y. X. & Lee, L. P. (2005) *Nano Lett.* **5,** 119–124.
32. Stuart, D. A., Yonzon, C. R., Zhang, X., Lyandres, O., Shah, N. C., Glucksberg, M. R., Walsh, J. T. & Duyne, R. P. V. (2005) *Anal. Chem.* **77,** 4013–4019.